

Non-contact, in-vivo, functional, and structural ophthalmic imaging using multimodal photoacoustic remote sensing (PARS) microscopy and optical coherence tomography (OCT)

Zohreh Hosseinaee¹, Nima Abbasi¹, Layla Khali¹, Lyazzat Mukhangaliyeva¹, Nicholas Pellegrino¹, Parsin Haji Reza^{1}*

1. PhotoMedicine Labs, Department of System Design Engineering, University of Waterloo, 200 University Ave W, Waterloo, ON, N2L 3G1, Canada

*Email: phajireza@uwaterloo.ca

Abstract

Early diagnosis of ocular diseases improves the understanding of pathophysiology and help with accurate monitoring and effective treatment. Advanced multimodal ocular imaging platforms play a crucial role in visualization of the ocular components and provide clinicians with a valuable tool for evaluating different eye diseases. Here, for the first time we present a non-contact, multimodal photoacoustic remote sensing (PARS) microscopy and swept-source optical coherence tomography (SS-OCT) for in-vivo functional and structural imaging of the eye. The system provides complementary imaging contrasts of optical absorption and optical scattering and is used for non-contact, in-vivo imaging of murine eye. Results of vasculature and structural imaging as well as melanin content in the retinal pigment epithelium (RPE) layer are presented. Multiwavelength PARS microscopy using Stimulated Raman Scattering (SRS) is applied for the first time, to provide non-contact oxygen saturation estimation in the ocular tissue. The reported work may be a major step toward clinical translation of the technology and has the potential to advance the diagnosis and treatment of ocular diseases.

1 Introduction

Ocular diseases adversely affect and even disable, normal functions of ocular tissue, and in some cases might lead to vision loss. Several studies have demonstrated the vital role of ocular blood oxygen saturation (sO_2) and melanin concentration in various prevalent eye diseases¹. Retinal oxygen saturation has been shown to be abnormal in diabetic retinopathy (DR)^{2,3}, glaucoma diseases^{4,5}, and retinal vein occlusions^{6,7}. In addition, RPE melanin loss is a major factor in progression of age-related macular degeneration (AMD)^{8,9}. The ability to precisely detect ocular sO_2 values and RPE melanin concentrations is crucial for improving investigations and diagnoses of major ocular diseases. In the past decades, extensive efforts have been made to accurately measure sO_2 and melanin concentration in the ocular environment. Invasive methods such as fluorescence imaging and oxygen-sensitive microelectrode

measurements, were used to measure the partial pressure of oxygen in retinal tissue^{10,11}, however, these methods are only suitable for pre-clinical animal studies. Multi-wavelength fundus photography and visible-light optical coherence tomography are among the other techniques used to measure retinal sO₂¹²⁻¹⁴. Despite having the advantage of being non-contact, the measurements made by these techniques are based on indirect methods and complex numerical models such as Lambert-Beer's Law^{15,16}. Moreover, they are sensitive to light scattering and local geometrical parameters, such as retinal thickness, vessel diameters, and retinal pigmentation, thus may result in biased estimations¹.

Among various medical imaging modalities, photoacoustic microscopy (PAM) offers the unique imaging contrast of optical absorption and enables direct measurement of chromophore's concentration inside the tissue. The technology is well-known for its functional and molecular imaging capabilities¹⁷. Over the past decades, photoacoustic ophthalmoscopy has been applied for visualizing hemoglobin and melanin content in ocular tissue¹⁸, quantifying ocular sO₂¹⁴, and measuring metabolic rate of oxygen consumption (MRO₂)¹⁹. Despite all these advantages offered by PAM devices, the major limitation arises from their need to be in contact with the ocular tissue²⁰. This physical contact might increase the risk of infection and may cause patient discomfort. Furthermore, this contact-based imaging approach applies pressure to the eye and introduces barriers to oxygen diffusion. Thus, it has a crucial influence on the physiological and pathophysiological balance of ocular vasculature function and it is not appropriate for studying dynamic processes under close condition to reality²¹.

In 2017 Haji Reza et al. developed photoacoustic remote sensing (PARS) microscopy for non-contact, non-interferometric detection of photoacoustic signals²². PARS microscopy can be considered as the non-contact, all-optical version of optical resolution PAM (OR-PAM), where the acoustically coupled ultrasound transducer is replaced with a co-focused detection beam. This all-optical detection scheme allows to measure the photoacoustic pressure waves at the subsurface origin where the pressure is maximum. The technology has proved its potential over a short period of time in various biomedical

applications such as label-free histology imaging^{23,24}, sO₂ mapping and angiogenesis imaging²⁵. Very recently, our group for the first time demonstrated non-contact, in-vivo photoacoustic imaging of ocular tissue using PARS microscopy and imaged the ocular vasculature in the mouse eye²⁶.

In ophthalmic imaging applications optical coherence tomography (OCT) is an state-of-the-art imaging technique extensively used in preclinical and clinical applications for imaging both anterior and posterior parts of the eye²⁷. Unlike photoacoustic imaging, OCT obtains its imaging contrast from optical scattering of internal tissue microstructures. OCT can be considered as an ideal companion for PARS microscopy by providing complementary imaging contrast for non-contact imaging of biological tissues. This multimodal imaging technology has the potential to provide chromophore selective image contrast in concert with depth-resolved scattering contrast²⁸. Martell et al.²⁹ reported a dual-modal PARS microscopy combined with spectral-domain OCT (SD-OCT) and applied it for in-vivo, non-contact imaging of mouse ear tissue.

Here for the first time, we have combined a multiwavelength PARS microscope system with a swept source OCT system (SS-OCT). The reason we have selected SS-OCT in our design is the extended imaging range, reduced sensitivity roll-off and improved light detection efficiency offered by SS-OCT system compared to SD-OCT counterparts. To our knowledge, this is the first time that a swept-source OCT system is combined with an OR-PAM system in general (both contact-based OR-PAM and non-contact OR-PAM). To achieve multiwavelength PARS microscopy Stimulated Raman Scattering (SRS) happening inside the optical fiber is used, and ocular images at multiple wavelengths are acquired and used for estimating sO₂ inside the tissue. Furthermore, for the first time we are showing the potential of PARS probe beam in providing scattering information of the imaged object. Therefore, the presented system provides a multimodal imaging platform offering non-contact optical absorption contrast through PARS microscopy, and non-contact optical scattering contrast through optical coherence tomography and PARS probe beam. The performance of the system for in-vivo imaging applications is demonstrated

by imaging mouse ear and ocular tissue. Additionally, for the first time, non-contact ocular sO₂ estimation is presented in living animal. The reported work has the potential to advance the diagnosis and treatment of ocular diseases.

2 Methods:

2.1 System Architecture

Figure 1 demonstrates the experimental setup of the multimodal PARS-OCT system. In the PARS subsystem a 532-nm 1 ns pulse-width, ytterbium-doped fiber laser (IPG Photonics) capable of pulse repetition rates from 20 kHz to 600 kHz is coupled to a 3.5-meter single mode optical fiber (PM460-HP, Thorlabs, Inc.) to generate SRS peaks. A fiber optic spectrometer (Thorlabs, Inc.) measured the SRS peaks and confirmed the filtered wavelengths. The output of the fiber was collimated, and bandpass filters (FB, Thorlabs Inc.) were used to select the desired wavelength. The detection arm uses an 830-nm Superluminescent Diodes with 20 nm full width at half maximum linewidth (SLD830S-A20, Thorlabs). The output end of the fiber is coupled to a collimator. A polarized beam splitter is used to transmit the majority of the forward light onto a quarter wave-plate, which transforms the linearly polarized light to circularly polarized light. The detection and excitation light are then combined using a dichroic mirror. The co-aligned beams are then directed toward a large beam galvanometer scanning mirror system (GVS012/M, Thorlabs, Inc.) driven by a two-channel function generator. The beams are then directed to a set of 1:1 telecentric pair that provides uniform image intensity and improves the effective FOV. A 0.4 NA refractive objective co-focused the beams onto the sample. The back-reflected light from the sample is collected via the same objective lens and guided towards the detection path. The quarter wave-plate transforms the reflected circularly polarized light back to linearly polarized light. This enables the polarized beam splitter to direct the back-reflected light towards the photodiode. A long-pass filter (FELH0800, Thorlabs Inc.) is used to block any residual 532 nm light. The 830 nm signal is then focused

with an aspherical lens onto a balanced photodiode. The balanced output of the photodiode is used to extract PARS signal and the monitor output provides the PARS scattering channel. The photodiode outputs are connected to a high-speed digitizer (CSE1442, Gage Applied, Lockport, IL, USA) that performs analog to digital signal conversion. A point acquisition is acquired for each pixel and recorded by the digitizer. Each point acquisition is converted to an intensity value by computing its maximum amplitude and plotted at its respective location in the image.

In the SS-OCT subsystem, a vertical cavity surface emitting laser (VCSEL) light source (Thorlabs, Inc.) is used as the light source. The laser is centered at ~ 1060 nm with 100 nm spectral bandwidth and frequency swept of 60 kHz. A-line trigger, i. e. sweep trigger was supplied by the light source. K-linear sampling clock was provided by the Mach-Zehnder interferometer-based clock module integrated within the laser³⁰. The output of the laser was connected to a custom fiber optic interferometer consisting of a circulator and a 50:50 fiber coupler that splits the light into the reference and sample arms. The reference arm consists of BK7 dispersion compensating prisms in the optical path and a translating mirror to set the zero delay. In the sample arm the collimated light is combined with the PARS excitation and probe beams and together are directed to the galvo-scanner mirrors. Depending on the application the numerical aperture of the microscope objective used for OCT system was switched between 0.14 and 0.4 which corresponds to ~ 15.6 μm and ~ 3.9 μm lateral resolution, respectively. The returning light from the sample and reference arms were interfered at the coupler and detected by built-in dual balanced photodetector. The OCT signal was digitized by a high-speed A/D card (ATS9351, Alazar Technologies Inc., Pointe-Claire, QC, Canada). The raw OCT data was transmitted to a host computer (Intel Core i-7) through a PCI-Express interface. OCT system control was implemented on MATLAB platform to automatically control all the operations including system calibration, galvo-scanning, system synchronization, real-time imaging preview and data acquisition.

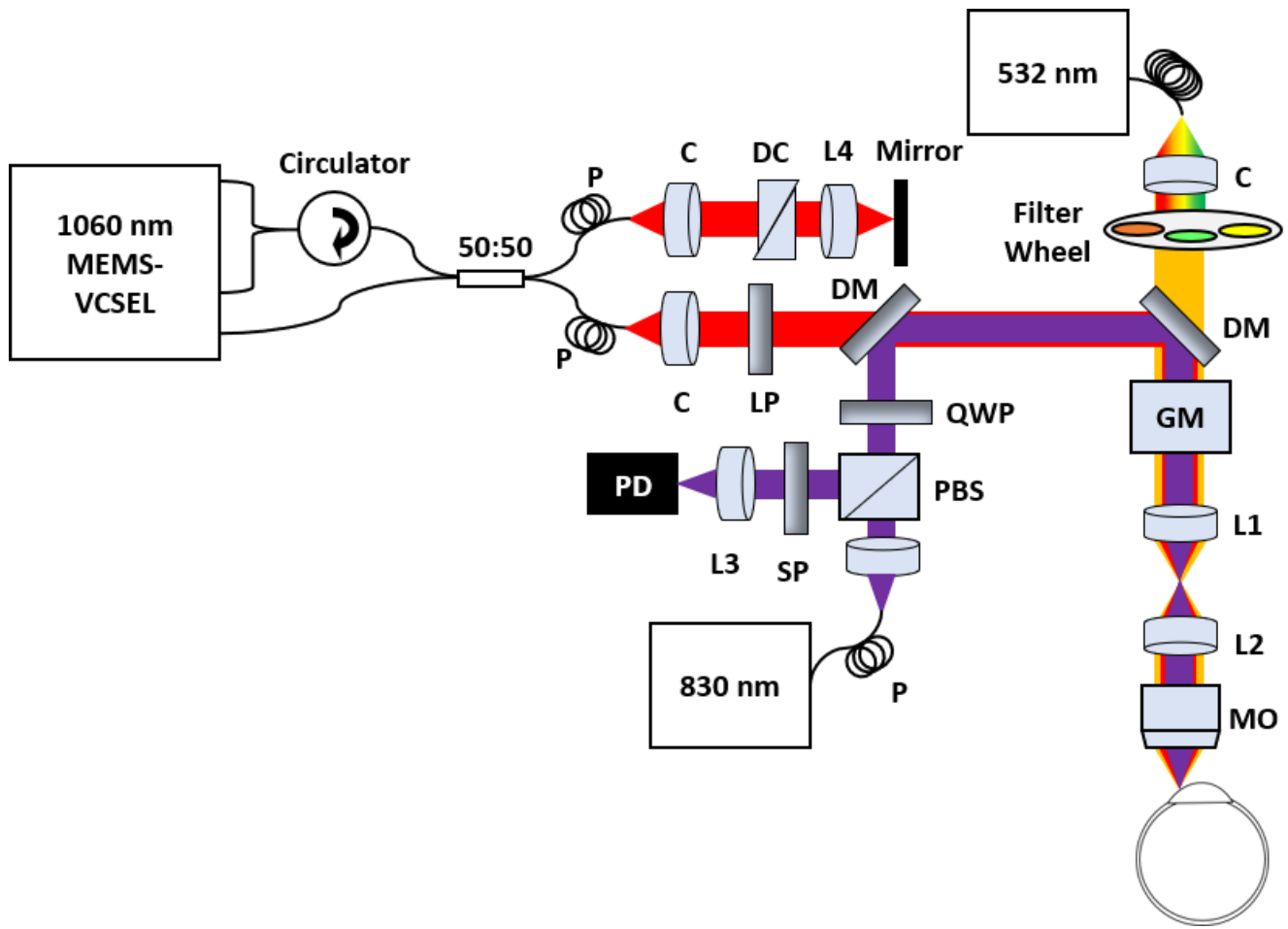


Figure 1: Simplified Schematic of the dual-modal PARS-OCT system. M: Mirror, DM: Dichroic mirror, QWP: Quarter wave plate, PBS: Polarized beamsplitter, LP: Long pass filter, GM: Galvanometer mirrors, MO: microscope objective, L: Lens, C: Collimator, PD: Photodiode. DC: Dispersion Compensation, P: Polarization controller.

2.2 Stimulated Raman Scattering

Stimulated Raman Scattering was used to generate multiple wavelengths required for sO₂ estimation³¹. To get SRS wavelengths, the output of the excitation laser was coupled into a 3.5-m polarization-maintaining single-mode fiber (PM-460 HP) using a fiber launch system (MBT621D/M, Thorlabs Inc.). The coupling efficiency for all these experiments was ~65%. A fiber optic spectrometer (Thorlabs, Inc.) was used to measure the SRS peaks and to confirm the filtered wavelengths. Table 1 shows the measured power at 100 KHz pulse repetition rate for 3.5-m fiber length.

Table 1: Measured power of SRS peaks generated in 3.5m fiber and at different 100KHz PRR.

3.5-m fiber (100 KHz)				
Generated Wavelength Energy	532 nm	545 nm	558 nm	573 nm
Output Energy (nJ)	250	230	230	180

2.3 *Image Reconstruction*

All the PARS images shown in this manuscript were formed using a maximum amplitude projection (MAP) of each A-scan as a pixel in an en-face image. The images were produced by direct plotting from interpolated raw data using a Delaunay triangulation interpolation algorithm³². All images and signal processing steps were performed in the MATLAB environment. Scale bars in the field of view (FOV) were calibrated using a 1951 USAF resolution test target.

For each OCT dataset, 500 A-lines were acquired for each B-scan and on each cross-sectional position the slow scan axis traversed through 500 lateral positions. For each A-line trigger, 2448 sampling points were acquired to cover the resultant spectral interferogram, providing a depth ranging distance of ~12 mm. As a pre-processing step to extract complex data, OCT reference spectrum was subtracted from interference signal to remove DC bias and then Fourier transform was performed, to extract depth-resolved OCT signal. The top half of Fourier transformed data was considered as the valid complex data for further processing. Images were generated from the raw OCT data and numerically dispersion compensated up to the 5th order with a custom MATLAB algorithm³³. No additional image post-processing was used for the OCT images presented in this paper. The volumetric and enface images were generated from the 3D data sets with ImageJ³⁴.

2.4 *Animal Preparation*

All of the experimental procedures were carried out in conformity with the laboratory animal protocol and was approved by the Research Ethics Committee at the University of Waterloo and adhered to the ARVO statement for use of animals in ophthalmic and vision research. Nude mice, and albino rats (NU/NU, Charles River, MA, USA) were imaged to demonstrate the in-vivo capabilities of the system. A custom-made animal holder was used to restrain the animal. The base of the animal holder was lined with a thermal pad in order to keep the animal body temperature between 36° and 38°C. Artificial tears were used frequently (~ every 5 minutes) to keep the cornea hydrated. Vital signs, such as respiration rates, heart rates and body temperature were monitored during the experiment.

2.5 Ocular light safety

Light safety is an important factor to consider in ocular imaging applications. In this study, the OCT light power on the cornea were measured to be ~1.5 mW centered at 1060 nm which is well within the ANSI safety limits for imaging human eye³⁵. For the PARS system the excitation pulse energy was in the range of 50-100 nJ and the detection power was ~ 2-3 mW. In ocular imaging the amount of maximum permissible exposure (MPE) depends on several factors including optical wavelength, pulse duration, and exposure aperture. For a single laser pulse at 532 nm, the maximum pulse energy should not exceed 200 nJ, assuming 7 mm pupil diameter in healthy human eye³⁶. The 50-100 nJ laser pulse energy range and detection power range used for PARS imaging are well within the ANSI safety limits and the 160 nJ safety limit reported by Tian et al.³⁷

3 **Results and Discussion**

The performance of the multimodal PARS-OCT system was evaluated by measuring system's spatial resolution and signal-to-noise ratio (SNR) and the test results are presented in Fig 2. The resolutions of PARS microscopy channels were characterized by imaging 0.97 μm diameter microbead solution. The lateral resolution of the PARS absorption contrast channel was measured $\sim 1.5 \pm 0.1 \mu\text{m}$, as shown in

Fig 2(A). The black line shows the raw data collected from the microbead, and the red line represents the first order Gaussian curve fit using MATLAB curve fitting toolbox. Similarly, the resolution of the scattering contrast channel was measured to be $\sim 3.1 \pm 0.1 \mu\text{m}$ (Fig 2B). The difference between the measured lateral resolutions can be justified by the difference between central wavelengths used in excitation (532 nm) and detection (830 nm) beams and also the beam size.

The OCT axial resolution was measured experimentally by using a mirror as the test sample and the result is shown in Fig 2(C). The red line PSF was measured after coarse hardware dispersion compensation unit in the reference arm. The black line PSF in Fig 2 (C) was measured after numerical dispersion compensation up to the 5th order using a custom MATLAB based algorithm. The FWHM of the axial PSF was 10.1 μm in free space, which corresponds to 7.3 μm in biological tissue, assuming an average refractive index of $n = 1.38$ and ignoring wavelength dependent local variation of the refractive index. Results from the system sensitivity test as a function of scanning depth are presented in Fig 2(D). The SNR of the system was measured using a mirror as the imaged object. The maximum SNR of 100 dB was measured at $\sim 100 \mu\text{m}$ away from the zero-delay line with incident power of $\sim 1.5 \text{ mW}$. The SNR roll-off in free space was measured to be $\sim 1\text{dB}$ over a scanning range of 1.3 mm.

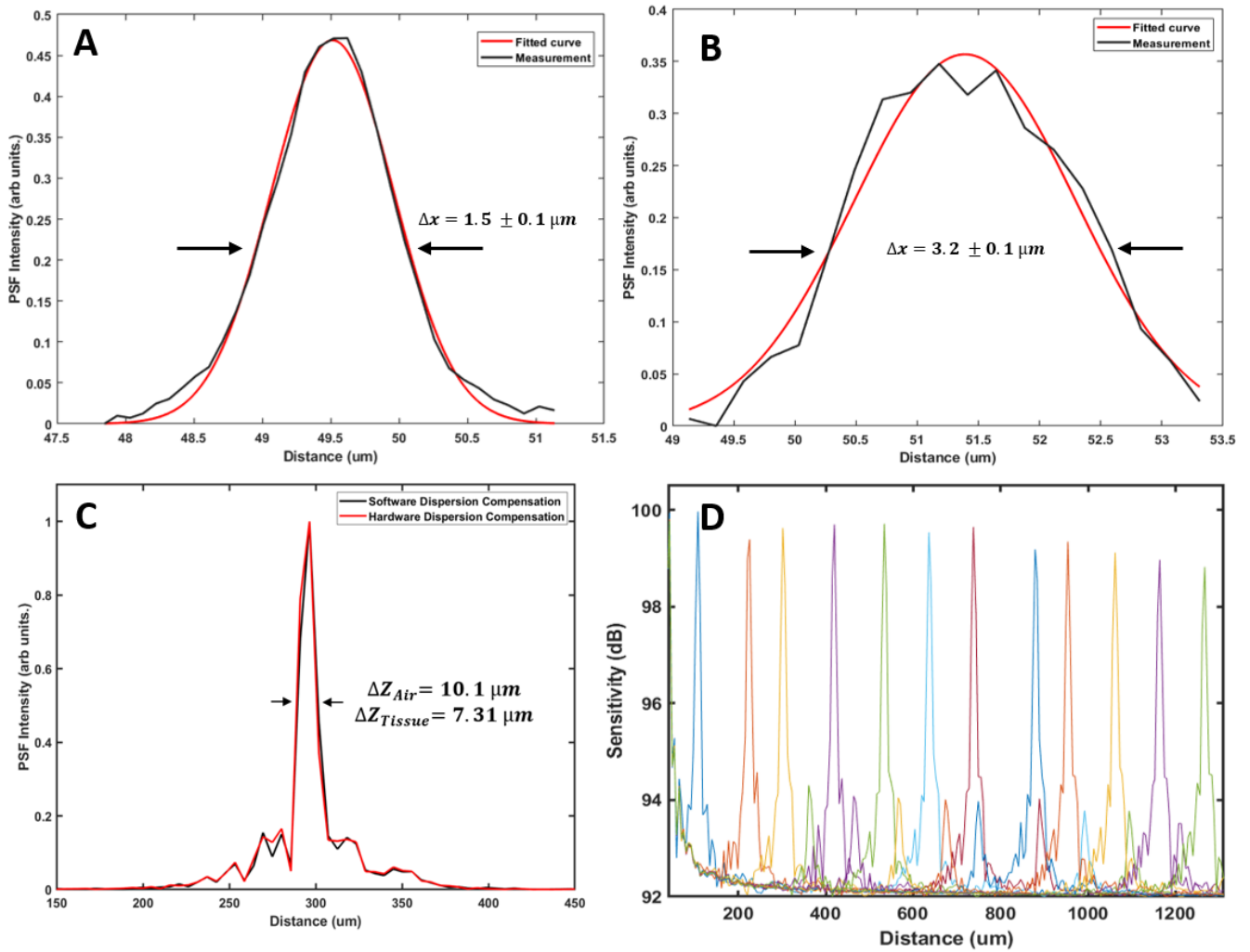


Figure 2: Point spread function (PSF) of PARS absorption channel characterized by imaging 0.97 μm diameter microbead solution (A). PSF of PARS scattering channel (B) Axial PSF of SS-OCT measured in free space (C). Sensitivity roll-off of SS-OCT (D).

The in-vivo performance of the multimodal optical imaging platform was first evaluated by imaging the mouse ear. Figure 3(A) demonstrates a rendering of a volumetric SS-OCT data set covering $\sim 2.5 \text{ mm} \times 2.5 \text{ mm}$ of the mouse ear. The volume consists of 500×500 axial scans and was acquired in 4 seconds. The side view of the volumetric SS-OCT data is presented in Fig. 3C, the cross-sectional B-scan of the dashed line is shown in (Fig 3D). Thanks to the axial resolution provided by the SS-OCT system, skin layers can be clearly seen in the ear tissue. The orthogonal view of the skin reveals the epidermis (E), which is the surface of the skin. The junction between epidermis and dermis is clearly visible followed by the dermis (D) where hair follicles, follicle shaft, follicle bulb, small blood and lymph vessels are

located. The dark layer inside the skin tissue is the auricular cartilage (AC) followed by adipose tissue (AT). En-face PARS images of microvasculature in the ear is presented in Figure 3B and shows vessels and small capillaries in the ear. Due to the shorter central wavelength used in PARS scattering channel (830 nm) compared to the OCT central wavelength (1060 nm), the achieved lateral resolution of PARS scattering channel is lower than the OCT system and enables seeing smaller structures like skin cells. En-face MAP image recorded by PARS scattering channel is shown in Fig 3E and visualizes skin cells (Figure 3E).

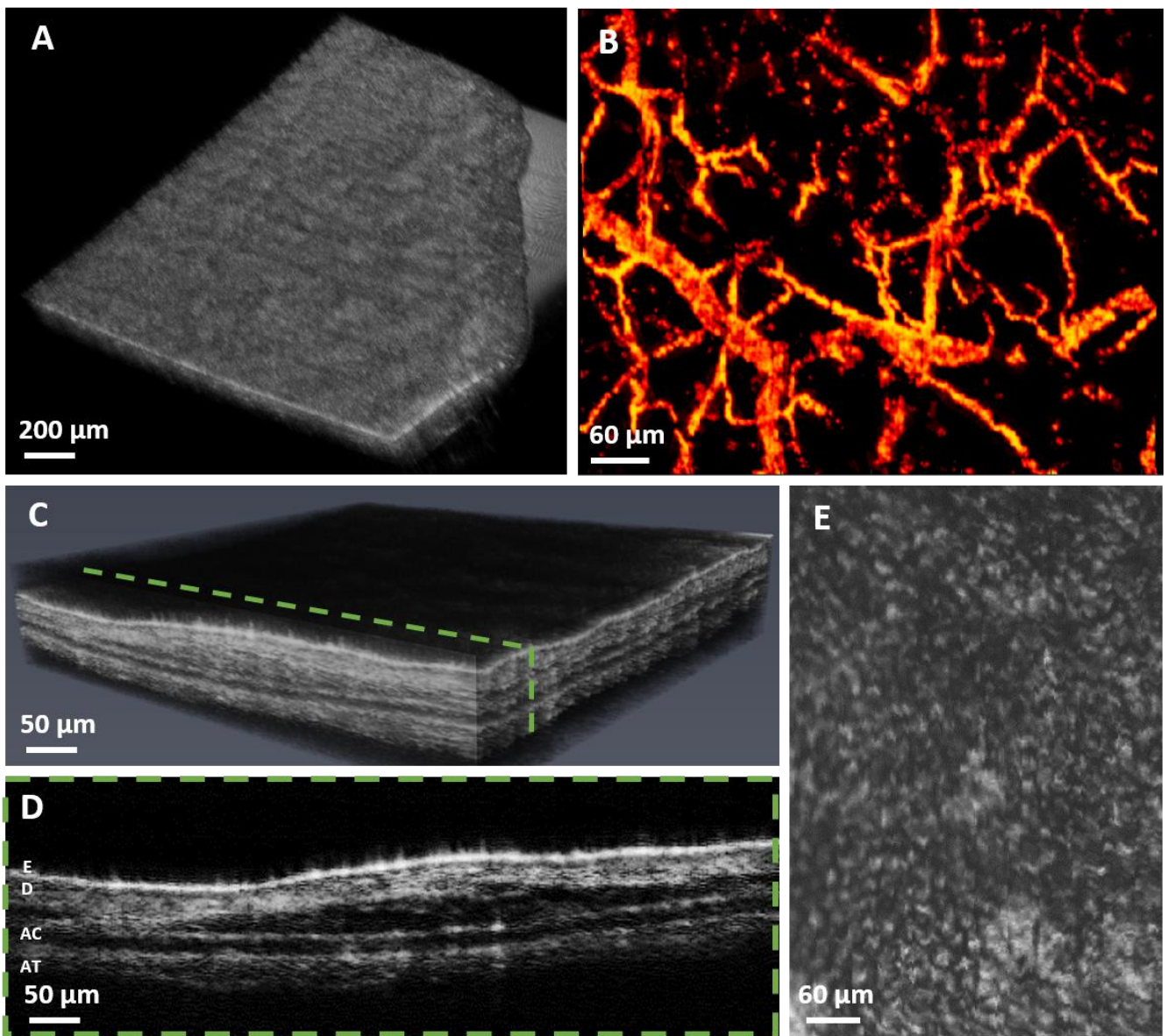


Figure 3: In-vivo imaging of mouse ear using dual-modal PARS-OCT system (A) Volumetric SS-OCT image, (B) Vasculature of the ear in a 600 mm × 600 mm area (C) Volumetric OCT image showing different layers inside the ear tissue. (D) Cross-sectional B-scan showing distinctive layers in the mouse ear tissue, E: Epidermis, D: Dermis, AC: Auricular cartilage AT: Adipose Tissue (E) Maximum amplitude projection image of the PARS scattering channel showing skin cells.

Figure 4 demonstrates representative images acquired using the multimodal PARS-OCT system in the ocular tissue. Figure 4(A) shows a rendering of a volumetric data set covering 7 mm × 7 mm area of the rat eye. The volume consists of 500 × 500 axial scans acquired in ~ 4 seconds. Figure 4(C) depicts a cut through a volumetric dataset acquired from the anterior segment showing the anterior segment anatomy. In Fig 4D the cross-sectional B-scan along the dashed-line in Fig 4C is shown which clearly demonstrates cornea, sclera, crystalline lens, and iris. Figure 4B depicts representative image acquired from iris vasculature using PARS microscopy. Capitalizing on the distinct difference in the absorption spectra of oxyhemoglobin HbO₂ and deoxyhemoglobin Hb, we used two excitation wavelengths (532 nm and 545 nm) to estimate the concentration of HbO₂ and Hb, thereby mapping the hemoglobin oxygen saturation sO₂ on a single vessel basis (dashed box in Fig 4B). Blood oxygenation levels are pseudocolored from red to blue in an ascending order. The spectroscopic advantage of PARS microscopy offers non-contact functional characterization of blood oxygenation.

The performance of PARS microscopy for imaging the other major optical absorber in ocular environment is shown in Figure 4 E & F by imaging melanin content in RPE and choroid layers. The PA signals coming from both layers contribute to the pixel intensity in the PARS absorption contrast image (Figure 4E) and PARS scattering contrast image (Fig 4F). The honeycomb shaped RPE cells can be appreciated in the images, however the motion artifacts have distorted part of the image.

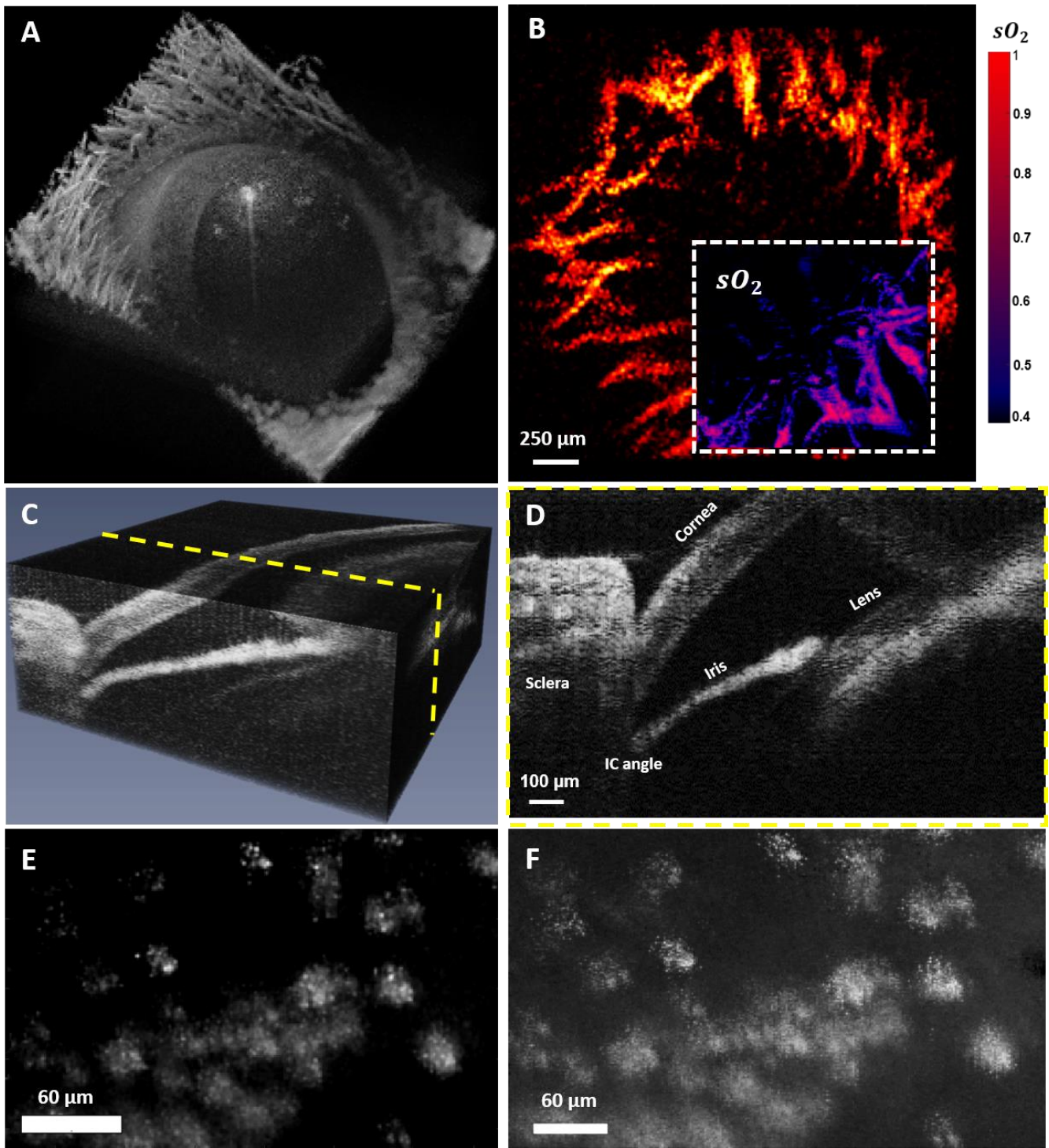


Figure 4: In-vivo imaging of ocular tissue using multimodal PARS-OCT (A) Rendering of a volumetric data set acquired from the rat eye (B) Iris vasculature imaged using PARS, along with sO_2 map (dashed box) on a single vessel basis (C) a cut through a volumetric dataset acquired from the anterior segment (D) the cross-sectional B-scan along the dashed-line in (C) demonstrating cornea, sclera, crystalline lens, and iris (E) Imaging melanin content in RPE and choroid layers using PARS absorption contrast channel, and (F) PARS scattering contrast channel.

4 Conclusions

The potential of multimodal PARS-OCT system for in-vivo, non-contact, multimodal imaging of ocular tissue was presented here. The presented multimodal system provides complementary imaging contrast of optical absorption and optical scattering. The capability of PARS microscopy for providing both absorption and scattering imaging contrasts was presented for the first time. The OCT system was used for showing depth-resolved structural information of biological tissue. The non-contact imaging ability offered by both systems makes them a favorable companion for clinical ophthalmic imaging applications. The system is a major step toward non-invasive, simultaneous, and accurate measurement of MRO_2 in the ophthalmic tissue and can assist ophthalmologists with the diagnostics and treatment of major eye diseases.

Acknowledgements:

The authors would like to thank Jean Flanagan for assistance with the animal-related procedures. The authors would also like to thank Kevan Bell, Benjamin Ecclestone, and Marian Boktor for their support and help. The authors acknowledge funding from New Frontiers in Research Fund – Exploration (NFRFE-2019-01012); Natural Sciences and Engineering Research Council of Canada (DGECR-2019-00143, RGPIN2019-06134); Canada Foundation for Innovation (JELF #38000); Mitacs (IT13594); Centre for Bioengineering and Biotechnology (CBB Seed fund); University of Waterloo and illumiSonics (SRA #083181).

Additional Information

Conflict of interest:

Author P.H. Reza has financial interests in illumiSonics Inc. IllumiSonics partially supported this work.

References

1. Liu, W. & Zhang, H. F. Photoacoustic imaging of the eye: A mini review. *Photoacoustics* **4**, 112–123 (2016).
2. Hammer, M. *et al.* Diabetic patients with retinopathy show increased retinal venous oxygen saturation. *Graefes Arch Clin Exp Ophthalmol* **247**, 1025–1030 (2009).

3. Khoobehi, B., Firn, K., Thompson, H., Reinoso, M. & Beach, J. Retinal Arterial and Venous Oxygen Saturation Is Altered in Diabetic Patients. *Invest. Ophthalmol. Vis. Sci.* **54**, 7103–7106 (2013).
4. Vandewalle, E. *et al.* Oximetry in glaucoma: correlation of metabolic change with structural and functional damage. *Acta Ophthalmologica* **92**, 105–110 (2014).
5. Olafsdottir, O. B., Hardarson, S. H., Gottfredsdottir, M. S., Harris, A. & Stefánsson, E. Retinal Oximetry in Primary Open-Angle Glaucoma. *Invest. Ophthalmol. Vis. Sci.* **52**, 6409–6413 (2011).
6. Hardarson, S. H. & Stefánsson, E. Oxygen Saturation in Central Retinal Vein Occlusion. *American Journal of Ophthalmology* **150**, 871–875 (2010).
7. Eliasdottir, T., Bragason, D., Hardarson, S. & Stefánsson, E. Retinal Oxygen Saturation is Affected in Central Retinal Vein Occlusion. *Invest. Ophthalmol. Vis. Sci.* **54**, 46–46 (2013).
8. HYMAN, L. G., LILIENFELD, A. M., FERRIS, F. L., III & FINE, S. L. SENILE MACULAR DEGENERATION: A CASE-CONTROL STUDY. *American Journal of Epidemiology* **118**, 213–227 (1983).
9. Landrum, J., Bone, R. & Kilburn, M. The macular pigment: A possible role in protection from age-related macular degeneration. **38**, 537–538 (1997).
10. Shonat, R. D. & Kight, A. C. Oxygen Tension Imaging in the Mouse Retina. *Annals of Biomedical Engineering* **31**, 1084–1096 (2003).
11. Wangsa-Wirawan, N. D. & Linsenmeier, R. A. Retinal oxygen: Fundamental and clinical aspects. *Archives of Ophthalmology* **121**, 547–557 (2003).
12. Harris, A., Dinn, R. B., Kagemann, L. & Rechtman, E. A Review of Methods for Human Retinal Oximetry. *Ophthalmic Surg Lasers Imaging Retina* **34**, 152–164 (2003).
13. Ramella-Roman, J. C. *et al.* Measurement of oxygen saturation in the retina with a spectroscopic sensitive multi aperture camera. *Opt. Express, OE* **16**, 6170–6182 (2008).

14. Chen, S., Yi, J. & Zhang, H. F. Measuring oxygen saturation in retinal and choroidal circulations in rats using visible light optical coherence tomography angiography. *Biomed Opt Express* **6**, 2840–2853 (2015).
15. Schweitzer, D., Thamm, E., Hammer, M. & Kraft, J. A new method for the measurement of oxygen saturation at the human ocular fundus. *International Ophthalmology* **23**, 347–353 (2001).
16. Human macular pigment assessed by imaging fundus reflectometry. *Vision Research* **29**, 663–674 (1989).
17. Yao, J. & Wang, L. V. Sensitivity of photoacoustic microscopy. *Photoacoustics* **2**, 87–101 (2014).
18. Shu, X., Li, H., Dong, B., Sun, C. & Zhang, H. F. Quantifying melanin concentration in retinal pigment epithelium using broadband photoacoustic microscopy. *Biomed. Opt. Express, BOE* **8**, 2851–2865 (2017).
19. Song, W. *et al.* A combined method to quantify the retinal metabolic rate of oxygen using photoacoustic ophthalmoscopy and optical coherence tomography. *Sci Rep* **4**, 6525 (2015).
20. Hosseinaee, Z., Le, M., Bell, K. & reza, P. H. Towards non-contact photoacoustic imaging [Review]. *Photoacoustics* 100207 (2020) doi:10.1016/j.pacs.2020.100207.
21. Link, D. *et al.* Novel non-contact retina camera for the rat and its application to dynamic retinal vessel analysis. *Biomed Opt Express* **2**, 3094–3108 (2011).
22. Hajireza, P., Shi, W., Bell, K., Paproski, R. J. & Zemp, R. J. Non-interferometric photoacoustic remote sensing microscopy. *Light: Science & Applications* **6**, e16278–e16278 (2017).
23. Ecclestone, B. R. *et al.* Improving maximal safe brain tumor resection with photoacoustic remote sensing microscopy. *Scientific Reports* **10**, 17211 (2020).
24. Ecclestone, B. R. *et al.* Towards virtual biopsies of gastrointestinal tissues using photoacoustic remote sensing microscopy. *Quantitative Imaging in Medicine and Surgery* **11**, 1070077–1071077 (2021).

25. Reza, P. H., Bell, K., Shi, W., Shapiro, J. & Zemp, R. J. Deep non-contact photoacoustic initial pressure imaging. *Optica* **5**, 814–820 (2018).
26. Hosseinaee, Z. *et al.* Label-free, non-contact, in vivo ophthalmic imaging using photoacoustic remote sensing microscopy. *Opt. Lett., OL* **45**, 6254–6257 (2020).
27. de Boer, J. F., Leitgeb, R. & Wojtkowski, M. Twenty-five years of optical coherence tomography: the paradigm shift in sensitivity and speed provided by Fourier domain OCT [Invited]. *Biomed. Opt. Express* **8**, 3248 (2017).
28. Hosseinaee, Z., Tummon Simmons, J. A. & Reza, P. H. Dual-Modal Photoacoustic Imaging and Optical Coherence Tomography [Review]. *Front. Phys.* **8**, (2021).
29. OSA | Multimodal imaging with spectral-domain optical coherence tomography and photoacoustic remote sensing microscopy. <https://www-osapublishing-org.proxy.lib.uwaterloo.ca/ol/abstract.cfm?uri=ol-45-17-4859>.
30. Ahsen, O. O. *et al.* Swept source optical coherence microscopy using a 1310 nm VCSEL light source. *Opt. Express, OE* **21**, 18021–18033 (2013).
31. Hajireza, P., Forbrich, A. & Zemp, R. In-Vivo functional optical-resolution photoacoustic microscopy with stimulated Raman scattering fiber-laser source. *Biomed. Opt. Express* **5**, 539 (2014).
32. Chen, L. & Xu, J. OPTIMAL DELAUNAY TRIANGULATIONS. *Journal of Computational Mathematics* **22**, 299–308 (2004).
33. Cense, B. *et al.* Ultrahigh-resolution high-speed retinal imaging using spectral-domain optical coherence tomography. *Opt. Express, OE* **12**, 2435–2447 (2004).
34. Schneider, C. A., Rasband, W. S. & Eliceiri, K. W. NIH Image to ImageJ: 25 years of image analysis. *Nature Methods* **9**, 671–675 (2012).

35. ANSI Z136.1-2014: Safe Use of Lasers - ANSI Blog. *The ANSI Blog*
<https://blog.ansi.org/2015/07/ansi-z1361-2014-safe-use-of-lasers/> (2015).
36. Jiao, S. *et al.* Photoacoustic ophthalmoscopy for in vivo retinal imaging. *Opt. Express* **18**, 3967 (2010).
37. Tian, C., Zhang, W., Mordovanakis, A., Wang, X. & Paulus, Y. M. Noninvasive chorioretinal imaging in living rabbits using integrated photoacoustic microscopy and optical coherence tomography. *Opt. Express* **25**, 15947 (2017).